

Article

A Nanoscale Cobalt Functionalized Strandberg-Type Phosphomolybdate with β -Sheet Conformation Modulation Ability in Anti-Amyloid Protein Misfolding

Man Wang ^{1,†}, Jiai Hua ^{1,*,†}, Pei Zheng ¹, Yuanzhi Tian ², Shaodan Kang ¹, Junjun Chen ¹, Yifan Duan ² and Xiang Ma ^{1,3,*} ¹ Chemistry and Chemical Engineering Department, Taiyuan Institute of Technology, Taiyuan 030008, China² Laboratory of Biochemistry and Pharmacy, Taiyuan Institute of Technology, Taiyuan 030008, China³ State Key Laboratory of Coordination Chemistry, Nanjing University, Nanjing 210023, China

* Correspondence: huaja@tit.edu.cn (J.H.); maxiang@tit.edu.cn (X.M.); Tel.: +86-351-3569476

† These authors contributed equally to this work.

Abstract: For decades, amyloid β -peptide ($A\beta$) misfolding aggregates with β -sheet structures have been linked to the occurrence and advancement of Alzheimer's disease (AD) development and progression. As a result, modulating the misfolding mode of $A\beta$ has been regarded as an important anti-amyloid protein misfolding strategy. A polyoxometalate based on $\{\text{Co}(\text{H}_2\text{O})_4\}^{2+}$ complex and $[\text{P}_2\text{Mo}_5\text{O}_{23}]^{6-}$ fragments, $\text{K}_8\{[\text{Co}(\text{H}_2\text{O})_4][\text{HP}_2\text{Mo}_5\text{O}_{23}]_2\}\cdot 8\text{H}_2\text{O}$ (abbreviated as CoPM), has been synthesized and structurally characterized using elemental analysis, single-crystal X-ray diffraction (SXRD), IR, UV spectra, bond valence sums (Σs) calculation, and powder XRD (PXRD). CoPM's primary component, as revealed by structural analysis, is a nanoscale polyoxoanion made of $[\text{Co}(\text{H}_2\text{O})_4]^{2+}$ sandwiched between two $[\text{P}_2\text{Mo}_5\text{O}_{23}]^{6-}$ pieces. Notably, it is demonstrated that CoPM efficiently modulates $A\beta$ aggregates' β -sheet-rich conformation.



Citation: Wang, M.; Hua, J.; Zheng, P.; Tian, Y.; Kang, S.; Chen, J.; Duan, Y.; Ma, X. A Nanoscale Cobalt Functionalized Strandberg-Type Phosphomolybdate with β -Sheet Conformation Modulation Ability in Anti-Amyloid Protein Misfolding. *Inorganics* **2023**, *11*, 442. <https://doi.org/10.3390/inorganics11110442>

Academic Editors: Kirill Grzhegorzhevskii and Wolfgang Linert

Received: 23 March 2023

Revised: 8 November 2023

Accepted: 15 November 2023

Published: 18 November 2023



Copyright: © 2023 by the authors. Licensee MDPI, Basel, Switzerland. This article is an open access article distributed under the terms and conditions of the Creative Commons Attribution (CC BY) license (<https://creativecommons.org/licenses/by/4.0/>).

Keywords: strandberg-type polyoxometalate; amyloid protein misfolding; conformation modulation; cobalt complexes

1. Introduction

Amyloid protein misfolding is linked to many disorders [1,2], with AD serving as a prevalent model for biochemistry and inorganic chemistry research [3]. The primary histopathological indicator of AD is the formation of extracellular senile plaques in the brain created by β -sheet-rich $A\beta$ [4–6]. Additionally, it has been shown that aberrant cerebral metal ions, such as Zn^{2+} , Cu^{2+} , and others, might encourage the misfolding aggregation of $A\beta$ [7,8]. Furthermore, the Cu^{2+} - $A\beta$ aggregates can generate reactive oxygen species (ROS), which is another causative factor in neuronal death [9]. As a result, controlling the detrimental misfolding aggregates may be key to treating these conditions [10–12].

Cobalt has long been recognized as a critical component of the human body, and the majority of its constituents, including cobalamin, have been linked to neuro-nutrition [13]. According to biochemical studies, the protein denaturation process may be significantly influenced by the strong coordination interaction between cobalt ions and nitrogenous heterocyclic compounds [14]. These properties may be useful for regulating the misfolding aggregates by substituting the inducing ions [15]. Finding the appropriate ligand is thus crucial for the creation of a complex that boosts both selectivity and steric hindrance to limit the active binding sites of cobalt.

Polyoxometalates (POMs), known as groups of metal–oxygen clusters, have multitudinous structures and intriguing characteristics [16–23]. POMs have several unique, unmatched characteristics that enable them to serve as substantial polydentate ligands for transition-metal ions with various coordination modes, such as oxygen-rich nucleophilic

surfaces, nanoscale sites, and sites that form multiple bonds [24–32]. Recently, it was shown that some nanoscale POMs, because of their distinct nanoscale size, high negative charge, and oxygen-rich surface, had a remarkable capacity for modifying misfolded β -sheet-rich conformation [33–36]. As a result, combining cobalt complexes with nanoscale POM clusters to create a single hybrid molecule may not only preserve but also advantageously express the desirable properties of all individual components.

In the present work, we have synthesized and studied a cobalt complex sandwiched phosphomolybdate, $K_8\{[Co(H_2O)_4][HP_2Mo_5O_{23}]_2\} \cdot 8H_2O$ (abbreviated as CoPM). The new molecular was fabricated from $[P_2Mo_5O_{23}]^{6-}$ partnered with $\{Co(H_2O)_4\}^{2+}$. As anticipated, CoPM can block $A\beta$'s β -sheet transformation. Furthermore, the decrease of Cu^{2+} -induced misfolded aggregates may reduce the formation of ROS.

2. Results and Discussion

2.1. X-ray Single Crystal Structures

In this study, the CoPM structure was determined using the SXRD method. Table S1 provides a list of bond lengths. Comprehensive data has been submitted to the Cambridge Crystallographic Data Centre (CCDC) under the CCDC number 2129591. The structural analysis results are shown in Figure 1a, which shows that the CoPM unit cell includes eight K^+ counter ions, eight crystallized water molecules, and one $\{Co(H_2O)_4\}^{2+}$ complex sandwiched polyoxoanion $[P_2Mo_5O_{23}]^{6-}$ (Figure 1a,b).

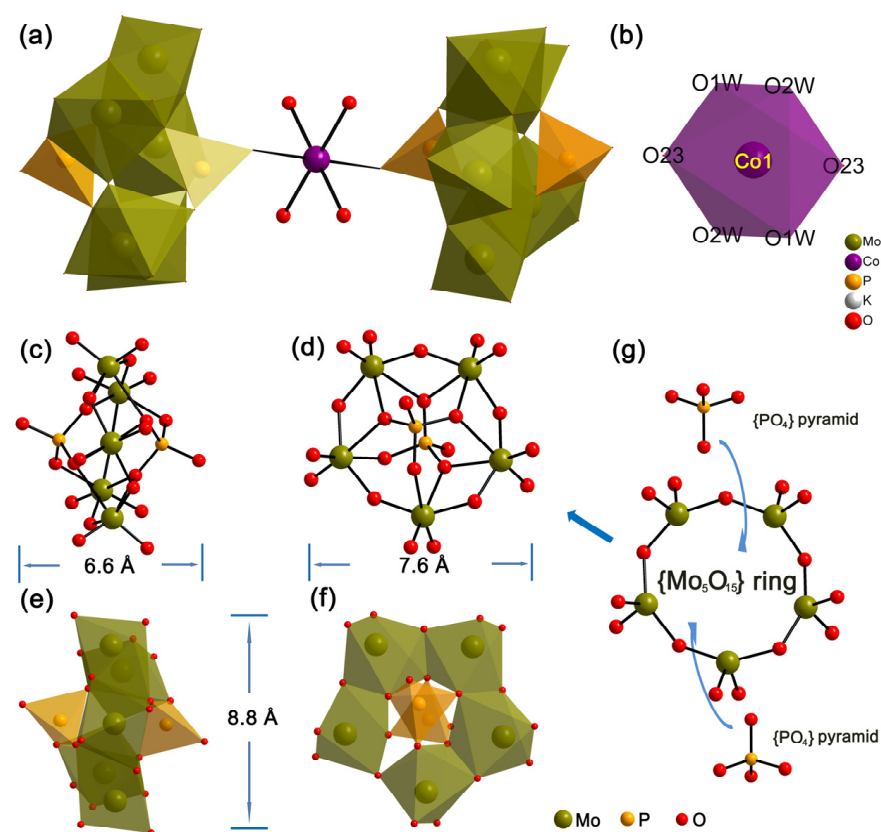


Figure 1. (a) A combined polyhedral/ball-and-stick representation of CoPM; (b) A polyhedral representation of $\{Co(H_2O)_4\}^{2+}$; (c,d) A ball-and-stick representation of the Strandberg-type fragment $\{[P_2Mo_5O_{23}]^{6-}\}$ via the X or Z axis; (e,f) Polyhedral Strandberg-type fragment via the X or Z axis; (g) Strandberg-type fragment's anatomical view.

As shown in Figure 1c–g, the geometry of Strandberg-type $[P_2Mo_5O_{23}]^{6-}$ cluster can be deemed as a puckered ring of five nearly coplanar corner-sharing/edge-sharing distorted MoO_6 octahedra [$Mo-O$: 1.679–2.496 Å] with two capping PO_4 tetrahedra [$P-$

O: 1.510–1.586 Å] on both poles of the $\{\text{Mo}_5\text{O}_{21}\}$ ring centers. Furthermore, two such $[\text{P}_2\text{Mo}_5\text{O}_{23}]^{6-}$ fragments were connected by a distorted octahedral $\{\text{Co}(\text{H}_2\text{O})_4\}^{2+}$ complex [Co–O: 2.035–2.179 Å] to form the polyanion structure of CoPM.

According to a retrieval of the CCDC database, CoPM's molecular structure is new. Hitherto, there are two similar POMs deposited in the CCDC database, $[\text{H}_8(\text{H}_2\text{O})_{16}][\text{Co}(\text{H}_2\text{O})_4(\text{HP}_2\text{Mo}_5\text{O}_{23})_2]$ (C1) [37] and $(\text{H}_2\text{en})_6\{[\text{Co}(\text{H}_2\text{O})_4](\text{P}_2\text{Mo}_5\text{O}_{23})\}_3 \cdot 11\text{H}_2\text{O}$ (C2) [38]. However, there are some differences among them: First of all, they have different molecular formulas. Second, CoPM is a salt rather than an acid. Third, CoPM possesses an isolated structure rather than a one-dimensional extended structure.

Additionally, the bond valence sums (Σs) in CoPM were computed using the following formula [39]:

$$V_i = \sum_j s_{ij} = \sum_j \exp\left(\frac{r_0' - r_{ij}}{B}\right) \quad (1)$$

In Formula (1), r_{ij} is the discovered bond distance provided in Table S1, and r_0' is the theoretical one between two atoms. The values for $r_0'(\text{Mo}^{6+}-\text{O})$ (1.903 Å), $r_0'(\text{P}^{5+}-\text{O})$ (1.624 Å), and $r_0'(\text{Co}^{2+}-\text{O})$ (1.698 Å) are from the literature [40,41]. B is defined as having a value of 0.349 [40]. As a consequence, Co, Mo, and P have average valence state sums (Σs) of 1.988, 5.956, and 4.925 in CoPM, respectively.

POMs are readily protonated because they have a lot of basic surface O atoms and strongly negatively charged pieces [42]. The 50 oxygen atoms in CoPM can be divided into bridging $\text{O}_{\mu 2}$, $\text{O}_{\mu 3}$, and $\text{O}_{\mu 4}$ types, respectively, as well as terminal O_t . As illustrated in Figure 2 and Table 1, according to the calculation of Σs , we can infer the distribution of protons on different oxygen atoms. Given that the oxidation state of O is -2 , we can derive the equation $\Sigma s + \Sigma H = 2$. Hence, the O atoms have delocalized protons with Σs values between 0 and 1.60, making them suitable as proton donors. Whereas O atoms with Σs values between 1.90 and 2.00 have dense electron populations. The numerous protons are often stated as being delocalized across the whole polyoxoanion, which is a common phenomenon in POM chemistry and has been extensively studied in the past, for example, $[\text{Ni}(\text{enMe})_2]_3[\text{H}_6\text{Ni}_{20}\text{P}_4\text{W}_{34}(\text{OH})_4\text{O}_{136}(\text{enMe})_8(\text{H}_2\text{O})_6] \cdot 12\text{H}_2\text{O}$ [39], $[\text{H}_3\text{W}_{12}\text{O}_{40}]^{5-}$ [42], $[\text{Cu}(\text{en})_2][\text{Cu}(\text{en})_2\text{H}_2\text{O}]_2\{[\text{Cu}(\text{en})_2][\text{Cu}_6(\text{en})_2(\text{H}_2\text{O})_2(\text{SiW}_9\text{O}_{34})_2]\} \cdot 8\text{H}_2\text{O}$ [43], and $[\text{Na}(\text{H}_2\text{O})_5]_2[\text{Ni}(\text{H}_2\text{O})(\text{en})_2]_2[\text{Ni}(\text{H}_2\text{O})_3(\text{en})][\text{H}_4\text{Ni}_6(\text{OH})_2(\text{en})_{2.5}(\text{B}-\alpha\text{-As}^{\text{V}}\text{W}_9\text{O}_{34})_2][\text{W}_4\text{O}_{16}][\text{Ni}_4(\text{H}_2\text{O})_2(\text{en})_2]_2[\text{Ni}(\text{H}_2\text{O})(\text{en})][(\alpha\text{-As}^{\text{V}}\text{W}_6\text{O}_{26})_2] \cdot 3\text{H}_2\text{O}$ [44].

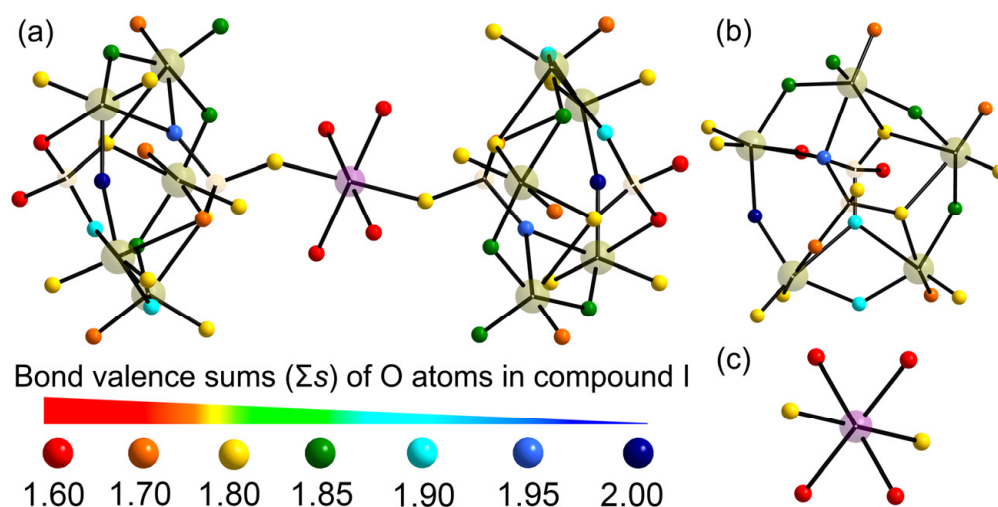


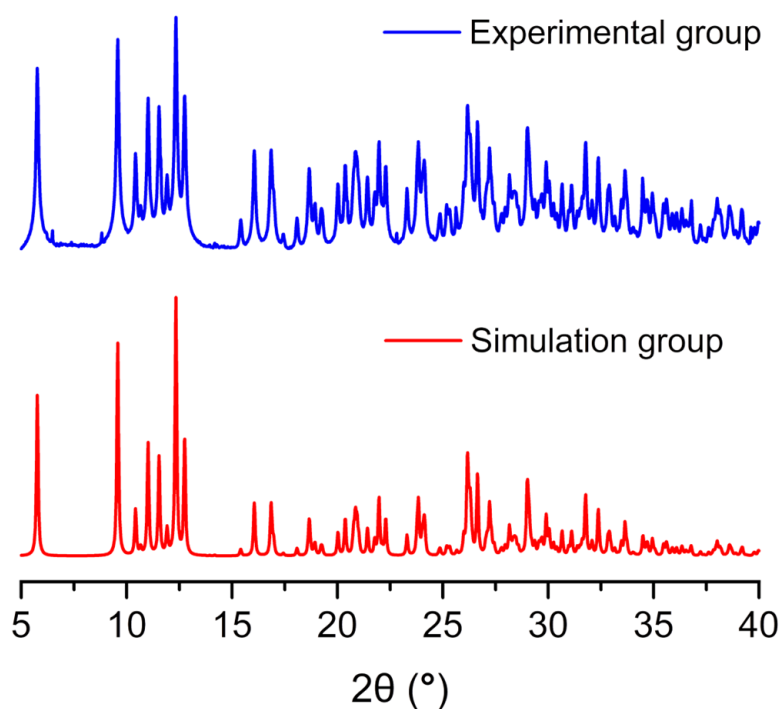
Figure 2. (a) Σs of O in the CoPM; (b) Σs values details of $[\text{P}_2\text{Mo}_5\text{O}_{23}]^{6-}$ skeleton; (c) Σs values details of $\{\text{Co}(\text{H}_2\text{O})_4\}^{2+}$. (Each O atom's Σs value is reflected by the color scheme).

Table 1. Bond valence and Σs of Mo, Co, and P in CoPM.

Bond	Valence	Bond	Valence	Bond	Valence	Atom	Σs
Mo(1)-O(1)	1.764	Mo(1)-O(15)	0.997	Mo(1)-O(16)	0.298		
Mo(1)-O(6)	1.689	Mo(1)-O(11)	0.910	Mo(1)-O(21)	0.262	Mo(1)	5.919
Mo(2)-O(2)	1.804	Mo(2)-O(12)	0.920	Mo(2)-O(19)	0.468		
Mo(2)-O(7)	1.709	Mo(2)-O(11)	0.912	Mo(2)-O(16)	0.183	Mo(2)	5.997
Mo(3)-O(8)	1.743	Mo(3)-O(13)	1.012	Mo(3)-O(19)	0.295		
Mo(3)-O(3)	1.719	Mo(3)-O(12)	0.905	Mo(3)-O(17)	0.268	Mo(3)	5.942
Mo(4)-O(4)	1.769	Mo(4)-O(13)	0.963	Mo(4)-O(20)	0.360		
Mo(4)-O(9)	1.719	Mo(4)-O(14)	0.879	Mo(4)-O(18)	0.252	Mo(4)	5.941
Mo(5)-O(5)	1.734	Mo(5)-O(14)	0.994	Mo(5)-O(18)	0.381		
Mo(5)-O(10)	1.694	Mo(5)-O(15)	0.867	Mo(5)-O(21)	0.310	Mo(5)	5.979
Co(1)-O(23)	0.408	Co(1)-O(1W)	0.308	Co(1)-O(2W)#5	0.278		
Co(1)-O(23)#5	0.408	Co(1)-O(1W)#5	0.308	Co(1)-O(2W)	0.278	Co(1)	1.988
P(1)-O(17)	1.308	P(1)-O(18)	1.231	P(1)-O(16)	1.272		
P(1)-O(22)	1.100					P(1)	4.911
P(2)-O(23)	1.331	P(2)-O(21)	1.156	P(2)-O(20)	1.301		
P(2)-O(19)	1.151					P(2)	4.939

2.2. PXRD, IR and UV-Visible Spectrum

By comparing the actual PXRD pattern with the simulated pattern from a single SXRD, the phase purity of CoPM was verified (see Figure 3).

**Figure 3.** Comparison of the CoPM PXRD patterns from simulation and experiment.

The IR spectrum of CoPM exhibits similar asymmetric those observed in other species containing $[P_2Mo_5O_{23}]^{6-}$ [45]. As shown in Figure 4, four characteristic spectral lines are assigned to $\nu(P-O_{\mu 4})$, $\nu(Mo-O_t)$, $\nu(Mo-O_{\mu 2})$, $\nu(Mo-O_{\mu 3})$ and $\nu(Mo-O_{\mu 4})$, respectively, and are situated at 1035, 933, 885, and 762~716 cm^{-1} , respectively [45]. Additionally, the stretching and bending vibrations of the -OH bond may be attributed to the corresponding spectral lines at 3460 and 1623 cm^{-1} , respectively [46]. The IR data were consistent with the structural elucidation from SXRD.

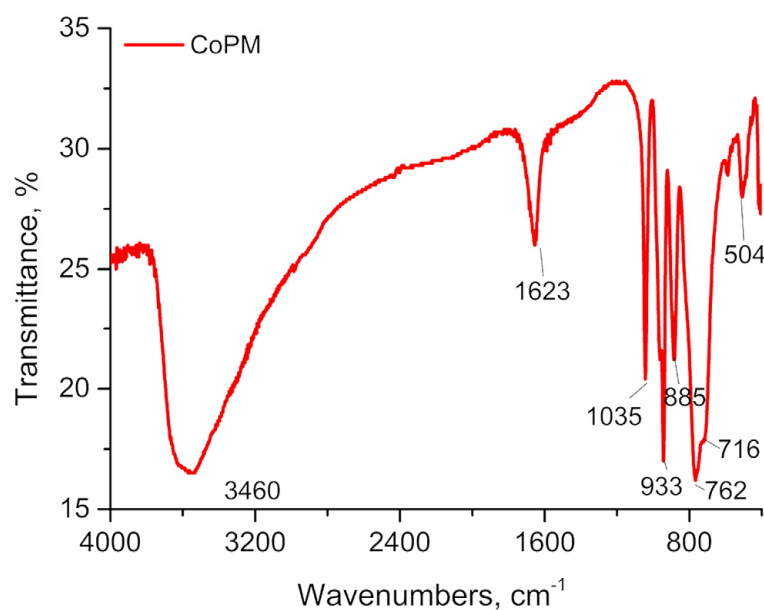


Figure 4. IR spectra for CoPM.

Figure 5 illustrates two UV-*vis* spectral absorption peaks in the wavelength range of 190–400 nm, one at 205.2 nm and the other with a broad shoulder adsorption center at 231.1 nm. These two peaks may be assigned to the $O_t \rightarrow Mo$ and $O_\mu \rightarrow Mo$ charge transfer transitions, respectively [47].

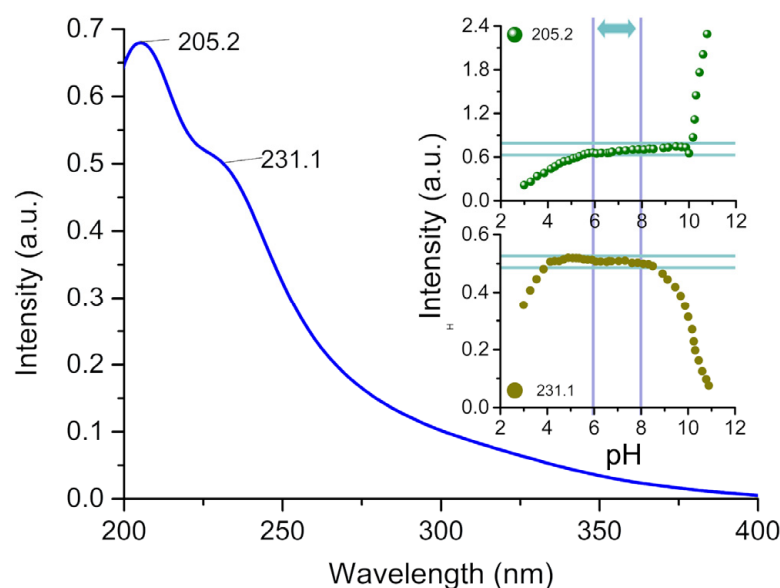


Figure 5. CoPM's UV-visible spectra in ultrapure water and its stability in a variety of pH values (adjusted by using $6.0 \text{ mol} \cdot \text{L}^{-1}$ HCl) are shown in the inset figure.

Utilizing UV-*vis* spectroscopy, the impact of pH value on the stability of CoPM has been further investigated. Within a pH range of roughly 6.0–8.0, insignificant variations in UV-*vis* absorption intensity are observed; the absorption peak intensities at 205.2 and 231.1 nm eventually alter outside of this range, suggesting the beginning of skeletal collapse inside the CoPM. Therefore, it may be concluded that the pH range for CoPM stability is between 6.0 and 8.0. The stability of CoPM in $\text{Cu}^{2+}/\text{Zn}^{2+}$ containing solution or in Tris-buffer is shown in Figure S1, Figure S2, and Figure S3, respectively.

2.3. Modulation of Conformation

Transmission electron microscopy (TEM) was used to examine Zn²⁺- or Cu²⁺-treated A β 40 with or without CoPM. Under self- or induction of Zn²⁺/Cu²⁺ conditions, certain fibrils can be detected in the groups of A β 40, A β 40 + Zn²⁺, and A β 40 + Cu²⁺ (Figure 6a–c), which is indicative of β -sheet-rich misfolding protein shape [48]. Additionally, the fibrils in the A β 40 + Zn²⁺ group are stronger after treatment with Zn²⁺ than those in the A β 40 + Cu²⁺ or A β 40 alone, which suggests that Zn²⁺ may exacerbate the β -sheet-relate conformational shift [49]. These findings show that the incubation fluids include abundant soluble “ β -sheet-rich A β .” A β 40 and A β 40 were treated with Zn²⁺ or Cu²⁺, however, great morphological changes when incubated with CoPM (Figure 6d–f). It is interesting to note that the shape of the A β 40 + CoPM group differs from that of A β 40 alone, suggesting that CoPM may also be able to prevent A β from misfolding on itself. According to reports, mono-functional chelators have no direct interactions with the A β peptide and can only stop metal ions from causing conformational misfolding. Therefore, they have no impact on the A β peptide’s self-misfolding [49]. These results may indicate that CoPM can serve as an interfering agent in the formation of β -sheets rather than a chelation agent.

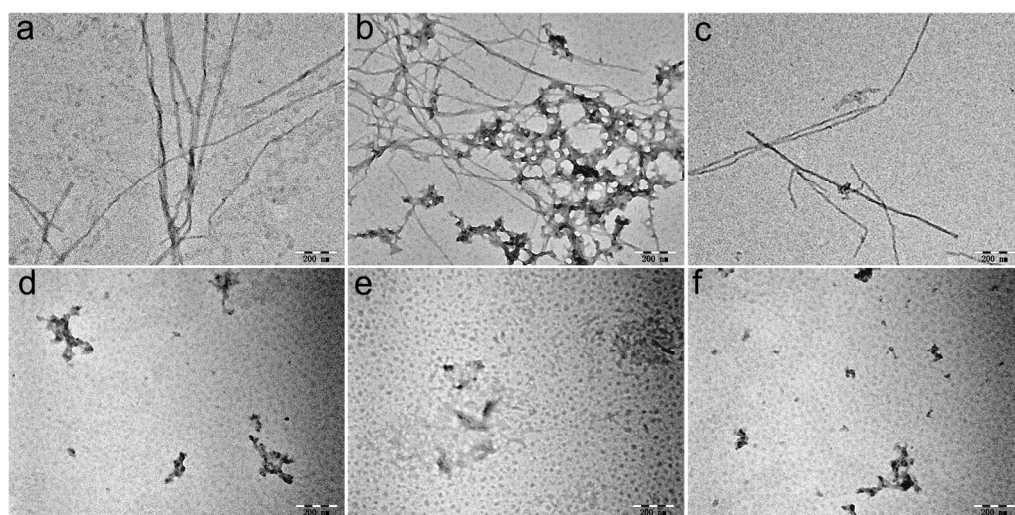


Figure 6. TEM images of A β 40 (20 μ M) incubated at 37 $^{\circ}$ C and pH 7.4 for 24 h with or without Zn²⁺, Cu²⁺ and CoPM. (a) A β 40; (b) A β 40 + Zn²⁺; (c) A β 40 + Cu²⁺; (d) A β 40 + CoPM; (e) A β 40 + Zn²⁺ + CoPM; (f) A β 40 + Cu²⁺ + CoPM ([A β 40]:[metal ion]:[CoPM] = 1:2:1). (The volume ratio for all samples with final DMSO concentration is 0.5%).

The Thioflavin T (ThT) assay was conducted to further examine the conformational modulation impact of CoPM on the fibrils of A β that are rich in β -sheets [50]. According to the amount of β -sheet-rich amyloid aggregates, the ThT may particularly attach to the β -sheet fibrils and cause a considerable enhancement in fluorescence, which has frequently been utilized to identify β -sheet content in incubation fluid [51]. As depicted in Figure 7, after one day of incubation at 37 $^{\circ}$ C with Zn²⁺, an A β 40 solution (20 μ M) exhibits significant fluorescence, demonstrating that the A β 40 primarily occurs in the β -sheet-rich conformation [51]. However, a steady drop in fluorescence intensity was seen when CoPM was present. Since CoPM possesses no ability to quench the fluorescence of ThT (shown in Figure S4), it would mean that CoPM can prevent the development of β -sheet-rich fibrils that Zn²⁺ induces. The same phenomena were also observed in another two groups, which is consistent with morphology experiment results.

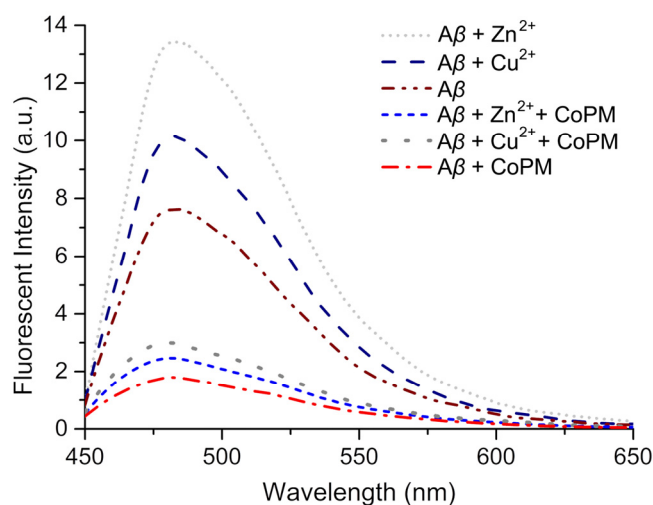


Figure 7. Thioflavin T (ThT) fluorescence spectra ($\lambda_{ex} = 415$ nm) of A β 40, A β 40 + Cu $^{2+}$, and A β 40 + Zn $^{2+}$ fibrils (20 μ M) after treated with CoPM at 37 °C and pH 7.4.

It has been established that the misfolding Cu $^{2+}$ -A β aggregates can be extremely effective in catalyzing ROS production [52]. Therefore, the DCF fluorescence test was conducted to further investigate the inhibitory impact of CoPM on ROS generation mediated by those Cu $^{2+}$ -A β species. Non-fluorescent 2', 7'-dichlorofluorescein (DCFH) is transformed into DCF by interacting with ROS in the presence of horseradish peroxidase (HRP), a fluorescent probe that can measure the system's total ROS output [53]. According to Figure 8, the DCF fluorescence intensity of Cu $^{2+}$ -A β and CoPM seems to be less intense than that of Cu $^{2+}$ -A β incubation alone, suggesting that the formation of ROS with CoPM is much lower than that without CoPM. These findings demonstrate that CoPM effectively inhibits Cu $^{2+}$ -A β complex ROS production [54]. Figure 8 shows that the Cu $^{2+}$ -A β plus Co $^{2+}$ group creates a significant amount of ROS, suggesting that the Co $^{2+}$ did not impact the experimental group's HRP activity. It is interesting to note that the H $_6$ P $_2$ Mo $_5$ O $_23$ (abbreviated as PM) Strandberg-type cluster is likewise capable of preventing ROS from modifying β -sheet-rich aggregates. We conclude that CoPM has a greater inhibitory impact than PM, suggesting that the unique structure of CoPM makes it have a higher modulation capacity.

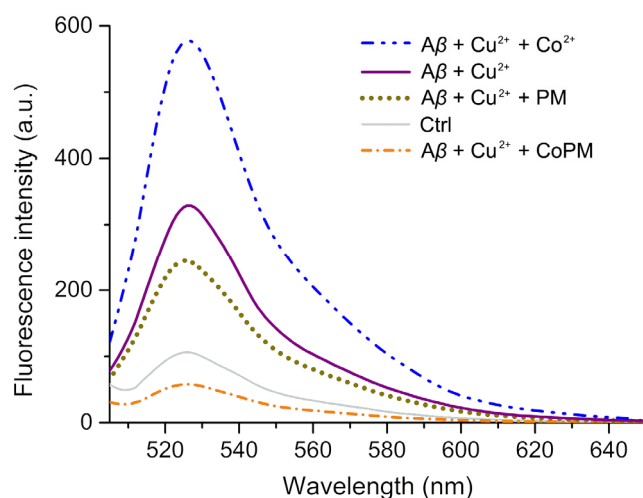


Figure 8. DCF fluorescence intensity at 485 nm, generated by Cu $^{2+}$ + A β + Co $^{2+}$, Cu $^{2+}$ + A β , Cu $^{2+}$ + A β + PM, Cu $^{2+}$ + A β + CoPM, and control group in Tris-buffer (20 mM Tris-HCl/150 mM NaCl, pH 7.4). (CoPM for K $_8$ {[Co(H $_2$ O) $_4$][HP $_2$ Mo $_5$ O $_23$] $_2$ }\cdot 8H $_2$ O, PM for H $_6$ P $_2$ Mo $_5$ O $_23$, Co $^{2+}$ for CoCl $_2$ \cdot 2H $_2$ O).

3. Materials and Methods

All of the reagents used in the present investigation were analytically pure and used exactly as they were given to us. DCFH-DA (2', 7'-dichlorofluorescein diacetate), HRP, tris(hydroxymethyl)aminomethane (Tris) were acquired from Sigma-Aldrich Inc. (Shanghai, China), whereas ascorbic acid, KCl, CuCl₂, ZnCl₂, CoCl₂·2H₂O, Na₂MoO₄·2H₂O, and Na₂HPO₄·12H₂O were bought from J & K Scientific Inc. (Beijing, China). Milli-Q water (Millipore, Burlington, MA, USA) was used to prepare all of the solutions, and a Millipore filter (0.22 μm) was used for all filtrations.

The Nicolet (Thermo Fisher Nicolet Inc., Waltham, MA, USA) 170 SX FTIR spectrometer was used to analyze the CoPM samples' spectra while scanning from 4000 to 400 cm⁻¹. A UV-3600 spectrometer was used to record UV spectra between 190 and 400 nm. DCF fluorescence was done using a Thermo (Thermo Fisher Scientific Inc., Singapore) Scientific Varioskan Flash microplate reader. The Edinburgh (Edinburgh instruments Inc., Edinburgh, UK) Raman spectrometer RM5 was used to test the fresh and recrystallized samples of CoPM before and after incubation with Tris buffer solution scanning from 200 to 2000 cm⁻¹ (λ_{ex} = 785 nm). Graphite monochromatized Mo Kα radiation (λ = 0.71073 Å) at 296 K was utilized to measure CoPM single crystal intensity using a Bruker (Bruker Inc., Saarbrücken, Saarland, Germany) Apex-2 diffractometer with the aid of a CCD detector.

3.1. Synthesis

Solutions A and B were prepared separately. Solution A: Na₂MoO₄·2H₂O (2.416 g, 10.00 mmol) and Na₂HPO₄·12H₂O (2.399 g, 6.70 mmol) were dissolved in water (30 mL) under stirring. Solution B: CoCl₂ (1.300 g, 10.00 mmol) and KCl (1.50 g, 0.20 mmol) were added to water (30 mL) under stirring. After 10 min, the resulting mixture of B was added to solution A. After 10 min, the resulting mixture of B was introduced into solution A. Before adjusting the pH to 5.0 with 6 mol·L⁻¹ HCl, the mixture was stirred for 10 min at room temperature (RT). The solution was then deposited in a Teflon reaction kettle at 150 °C for four days. After 5 °C/h of programmed cooling, 28% of K₈{[Co(H₂O)₄][HP₂Mo₅O₂₃]₂}·8H₂O crystals were obtained from Na₂MoO₄·2H₂O.

3.2. X-ray Crystallography

Utilizing graphite monochromatized Mo Kα radiation (λ = 0.71073 Å) at 296 K, a single crystal was put in an Apex-2 diffractometer (Bruker) with a CCD detector. For data integration, Bruker's SAINT software (Version 6.02A) suite was used. Corrections for polarization and Lorentz were applied according to protocol [55]. The SADABS software (Version 5.624) suite (Bruker) was used to perform adsorption adjustments using the multi-scan method [56]. The full-matrix least-squares approach enhanced F2's structure after being directly solved. This same refinement was performed successively along with Fourier syntheses for the remaining atoms. SHELXL-97 (Georg-August-Universität Göttingen, 2014, University of Göttingen, Göttingen, Niedersachsen, Germany) was used for calculations [57]. The locations of any hydrogen atoms connected to the water molecule were not shown on the Fourier difference map. Hydrogen atoms coupled to C and N were placed geometrically. All of the hydrogen atoms underwent isotropic refinement using the riding model and SHELXL's default settings. The crystal information and structural refinement processes for CoPM are listed in Table 2.

Table 2. Crystal data and structure refinements for CoPM.

Empirical Formula	H ₂₄ CoK ₈ Mo ₁₀ O ₅₈ P ₄
Formula weight	2407.20
Crystal system	Triclinic
Space group	P-1
a/Å	9.486(3)
b/Å	10.270(3)
c/Å	15.597(4)

Table 2. Cont.

Empirical Formula	H ₂₄ CoK ₈ Mo ₁₀ O ₅₈ P ₄
α /deg	94.275(4)
β /deg	97.073(4)
γ /deg	114.840(4)
$V/\text{\AA}^3$	1355.0(6)
Z	1
$D_c/\text{g cm}^{-3}$	2.950
μ/mm^{-1}	3.391
T/K	296(2)
Limiting indices	$-11 \leq h \leq 11$ $-9 \leq k \leq 12$ $-18 \leq l \leq 16$
Measured reflections	6895
Independent reflections	4721
R_{int}	0.0149
Data/restraints/parameters	4721/0/376
GOF on F^2	1.051
Final R indices [$I > 2\sigma(I)$]	$R_1 = 1.051$ $wR_2 = 0.0686$
R indices (all data)	$R_1 = 0.0264$ $wR_2 = 0.0698$

3.3. ThT Fluorescence Assay

In Tris buffer solution (20 mM Tris-HCl/150 mM NaCl, 990 μL), A β 40 (20 μM) was incubated with Zn(OAc)₂ (4 μL , 10 mM). The samples were subsequently incubated with CoPM (20 μM) or DMSO (1.5 μL) at 37 °C for 24 h. A Corning Costar Corp. flat-bottomed 96-well black plate received each 300 μL sample. Each well received 2 μL of 5 mM ThT solution in the darkness and subjected to incubation for 1 h at 37 °C. The Thermo Scientific Varioskan Flash microplate reader was used to detect fluorescence intensity ($\lambda_{\text{ex}} = 415 \text{ nm}$).

3.4. Morphological Analysis

Identical to the ThT fluorescence test, samples were prepared. On the 300-mesh copper grids with carbon coatings, 10 μL of the solution was seen at RT. The extra solution was drained after 2 min. After 2 min uranyl acetate (10 μL , 1%, *w/v*) staining, the grids were rinsed with 10 μL of Milli-Q water. A JEOL JEM-2100 LaB6 (HR) TEM was used to analyze the samples.

3.5. Inhibition of ROS Generation

Following the instructions in the report [58], the HRP stock solution (4 μM) and the DCF stock solution (1 mM) were prepared using a Tris buffer (20 mM Tris-HCl/150 mM NaCl, pH 7.4). CuCl₂ (40 μM) and A β 40 (20 μM) samples were incubated at 37 °C with or without CoPM (20 μM , with a final DMSO concentration of 1.5 μL). Each sample was then added with 10 μM of ascorbate solution, which was then incubated for 10 min at 37 °C. The 96 wells of a black plate with a flat bottom received the samples (200 μL) via injection. After that, each solution received injections of DCF (100 μM) and HRP (0.04 μM), which were subsequently incubated at 37 °C in the dark. Thermo Scientific's Varioskan Flash microplate reader was used to detect the fluorescence intensity ($\lambda_{\text{ex}} = 485 \text{ nm}$).

4. Conclusions

Misfolded protein accumulation is a critical factor involved in the onset and progression of AD. The toxic species' essential structure is an A β in a β -sheet form created by the misfolding aggregation process. Furthermore, ROS generated by toxic aggregates is a crucial neurodegenerative factor. This study describes the synthesis and characterization of a novel cobalt complex functionalized phosphomolybdate K₈[Co(H₂O)₄][HP₂Mo₅O₂₃]₂·8H₂O

(CoPM). CoPM displays a sandwich-type structure, with two Strandberg-type fragments $[P_2Mo_5O_{23}]^{6-}$ linked by $\{Co(H_2O)_4\}^{2+}$ in the solid state. Because POM fragments and Co complexes interact synergistically, CoPM can modulate conformation. As a conformational modulator, CoPM can prevent A β from aggregating, thus inhibiting Cu $^{2+}$ -A β species to produce ROS. Due to its novel structure and advantageous features, CoPM is predicted to have a wide variety of potential applications in coordination chemistry and bio-inorganic chemistry investigations.

Supplementary Materials: The following supporting information can be downloaded at: <https://www.mdpi.com/article/10.3390/inorganics11110442/s1>, Table S1: Selected bond lengths (Å) for CoPM; Figure S1: IR spectra for CoPM before and after incubated with Cu $^{2+}$ and Zn $^{2+}$ (with a molar ratio of 1:2); Figure S2: (a) IR spectra for CoPM before and after incubated with Tris buffer solution (20 mM Tris-HCl/150 mM NaCl, with 5% DMSO); (b,c) Partial magnification of CoPM's IR spectra before and after incubation; Figure S3: Raman spectra for CoPM before (a) and after incubated (b) with Tris buffer solution (20 mM Tris-HCl/150 mM NaCl, with 5% DMSO); Figure S4: The fluorescence spectra ($\lambda_{ex} = 415$ nm) of Thioflavin T (ThT) with or without CoPM. (inset: the structural diagram of ThT).

Author Contributions: J.H. and X.M. conceived the idea of the research. X.M. designed the molecule. J.H. and M.W. synthesized the molecule. X.M., M.W., P.Z. and Y.T. designed and conducted the experiments. J.H., S.K., J.C. and Y.D. analyzed the data. All authors have read and agreed to the published version of the manuscript.

Funding: This research was funded by the Shanxi Province Science Foundation (No. 20210302124333), the Shanxi Province Collegiate Education Innovation Project (J20231305), the Fund for Shanxi "1331" Project, the Research Foundation of the Chinese State Key Laboratory of Coordination Chemistry (SKLCC2204), and Taiyuan Institute of Technology Scientific Research Initial Funding.

Data Availability Statement: Detailed information on CoPM has been deposited at the Cambridge Crystallographic Data Centre with a CCDC number of 2129591.

Conflicts of Interest: The authors declare no conflict of interest.

References

1. Silva, J.L. Ligand binding and hydration in protein misfolding: Insights from studies of prion and p53 tumor suppressor proteins. *Acc. Chem. Res.* **2010**, *43*, 271–279. [[CrossRef](#)] [[PubMed](#)]
2. Khan, A.N.; Khan, R.H. Protein misfolding and related human diseases: A comprehensive review of toxicity, proteins involved, and current therapeutic strategies. *Int. J. Biol. Macromol.* **2022**, *223*, 143–160. [[CrossRef](#)] [[PubMed](#)]
3. Kepp, K.P. Bioinorganic chemistry of Alzheimer's disease. *Chem. Rev.* **2012**, *112*, 5193–5239. [[CrossRef](#)]
4. Vinters, H.V. Emerging concepts in Alzheimer's disease. *Annu. Rev. Pathol. Mech. Dis.* **2015**, *10*, 291–319. [[CrossRef](#)]
5. Walsh, D.M.; Selkoe, D.J. A β Oligomers—a decade of discovery. *J. Neurochem.* **2007**, *101*, 1172–1184. [[CrossRef](#)]
6. Saravanan, K.M.; Zhang, H.P.; Zhang, H.L.; Zhang, H.L.; Xi, W.H.; Wei, Y.J. On the conformational dynamics of β -amyloid forming peptides: A computational perspective. *Front. Bioeng. Biotechnol.* **2020**, *8*, 532. [[CrossRef](#)] [[PubMed](#)]
7. Faller, P.; Hureau, C.; La Penna, G. Metal Ions and Intrinsically Disordered Proteins and Peptides: From Cu/Zn Amyloid- β to General Principles. *Acc. Chem. Res.* **2014**, *47*, 2252–2259. [[CrossRef](#)]
8. Bagheri, S.; Saboury, A.A.; Haertlé, T.; Rongioletti, M.; Saso, L. Probable reasons for neuron copper deficiency in the brain of patients with Alzheimer's disease: The complex role of amyloid. *Inorganics* **2022**, *10*, 6. [[CrossRef](#)]
9. Gaggelli, E.; Kozłowski, H.; Valensin, D.; Valensin, G. Copper homeostasis and neurodegenerative disorders (Alzheimer's, prion, and Parkinson's diseases and amyotrophic lateral sclerosis). *Chem. Rev.* **2006**, *106*, 1995–2044. [[CrossRef](#)]
10. Selkoe, D.J. Resolving controversies on the path to Alzheimer's therapeutics. *Nat. Med.* **2011**, *17*, 1060–1065. [[CrossRef](#)]
11. Chimon, S.; Shaibat, M.A.; Jones, C.R.; Calero, D.C.; Aizezi, B.; Ishii, Y. Evidence of fibril-like β -sheet structures in a neurotoxic amyloid intermediate of Alzheimer's β -amyloid. *Nat. Struct. Mol. Biol.* **2007**, *14*, 1157–1164. [[CrossRef](#)] [[PubMed](#)]
12. Du, Z.; Li, M.; Ren, J.S.; Qu, X.G. Current strategies for modulating A β aggregation with multifunctional agents. *Acc. Chem. Res.* **2021**, *54*, 2172–2184. [[CrossRef](#)]
13. Matthews, R.G. Cobalamin-Dependent Methyltransferases. *Acc. Chem. Res.* **2001**, *34*, 681–689. [[CrossRef](#)] [[PubMed](#)]
14. Bandarian, V.; Matthews, R.G. Quantitation of Rate Enhancements Attained by the Binding of Cobalamin to Methionine Synthase. *Biochemistry* **2001**, *40*, 5056–5064. [[CrossRef](#)]
15. Ma, X.; Hua, J.A.; Wang, K.; Zhang, H.M.; Zhang, C.L.; He, Y.F.; Guo, Z.J.; Wang, X.Y. Modulating conformation of A β -peptide: An effective way to prevent protein-misfolding disease. *Inorg. Chem.* **2018**, *57*, 13533–13543. [[CrossRef](#)]

16. Du, D.Y.; Qin, J.S.; Li, S.L.; Su, Z.M.; Lan, Y.Q. Recent advances in porous polyoxometalate-based metal-organic framework materials. *Chem. Soc. Rev.* **2014**, *43*, 4615–4632. [[CrossRef](#)] [[PubMed](#)]
17. Huang, J.L.; Lin, L.Q.; Sun, D.H.; Chen, H.M.; Yang, D.P.; Li, Q.B. Bio-inspired synthesis of metal nanomaterials and applications. *Chem. Soc. Rev.* **2015**, *44*, 6330–6374. [[CrossRef](#)]
18. Song, Y.F.; Tsunashima, R. Recent advances on polyoxometalate-based molecular and composite materials. *Chem. Soc. Rev.* **2012**, *41*, 7384–7402. [[CrossRef](#)]
19. Yang, K.; Ying, Y.X.; Cui, L.L.; Sun, J.C.; Luo, H.; Hu, Y.Y.; Zhao, J.W. Stable aqueous Zn–Ag and Zn–polyoxometalate hybrid battery driven by successive Ag⁺ cation and polyoxoanion redox reactions. *Energy Storage Mater.* **2021**, *34*, 203–210. [[CrossRef](#)]
20. Hua, J.A.; Wei, X.M.; Li, Y.F.; Li, L.Z.; Zhang, H.; Wang, F.; Zhang, C.L.; Ma, X. A cyclen-functionalized cobalt-substituted sandwich-type tungstoarsenate with versatility in removal of methylene blue and anti-ROS-sensitive tumor cells. *Molecules* **2022**, *27*, 6451. [[CrossRef](#)]
21. Zheng, K.T.; Niu, B.X.; Lin, C.M.; Song, Y.Z.; Ma, P.T.; Wang, J.P.; Niu, J.Y. DL-Serine covalently modified multinuclear lanthanide-implanted arsenotungstates with fast photochromism. *Chin. Chem. Lett.* **2023**, *34*, 107238. [[CrossRef](#)]
22. Mirzaei, M.; Eshtiagh-Hosseini, H.; Alipour, M.; Frontera, A. Recent developments in the crystal engineering of diverse coordination modes (0–12) for Keggin-type polyoxometalates in hybrid inorganic–organic architectures. *Coord. Chem. Rev.* **2014**, *275*, 1–18. [[CrossRef](#)]
23. Chen, H.; Zheng, K.; Wang, J.; Niu, B.; Ma, P.; Wang, J.; Niu, J. Discovery and isolation of two arsenotungstate species: [As₄W₄₈O₁₆₈]³⁶⁻ and [As₂W₂₁O₇₇(H₂O)₃]²²⁻. *Inorg. Chem.* **2023**, *62*, 3338–3342. [[CrossRef](#)] [[PubMed](#)]
24. Gong, C.H.; Zeng, X.H.; Zhu, C.F.; Shu, J.H.; Xiao, P.X.; Xu, H.; Liu, L.C.; Zhang, J.Y.; Zeng, Q.D.; Xie, J.L. A series of organic–inorganic hybrid materials consisting of flexible organic amine modified polyoxomolybdates: Synthesis, structures and properties. *RSC Adv.* **2016**, *6*, 106248–106259. [[CrossRef](#)]
25. Jin, H.J.; Zhou, B.B.; Yu, Y.; Zhao, Z.F.; Su, Z.H. Inorganic–organic hybrids constructed from heteropolymolybdate anions and copper–organic fragments: Syntheses, structures and properties. *CrystEngComm* **2011**, *13*, 585–590. [[CrossRef](#)]
26. Weng, J.B.; Hong, M.C.; Liang, Y.C.; Shi, Q.; Cao, R. A nucleobase–inorganic hybrid polymer consisting of copper bis(phosphopentamolybdate) and cytosine. *J. Chem. Soc. Dalton Trans.* **2002**, *3*, 289–290. [[CrossRef](#)]
27. Meng, J.X.; Lu, Y.; Li, Y.G.; Fu, H.; Wang, E.B. Controllable self-assembly of four new metal–organic frameworks based on different phosphomolybdate clusters by altering the molar ratio of H₃PO₄ and Na₂MoO₄. *CrystEngComm* **2011**, *13*, 2479–2486. [[CrossRef](#)]
28. Xu, X.X.; Gao, X.; Lu, T.T.; Liu, X.X.; Wang, X.L. Hybrid material based on a coordination-complex-modified polyoxometalate nanorod (CC/POMNR) and PPy: A new visible light activated and highly efficient photocatalyst. *J. Mater. Chem. A* **2015**, *3*, 198–206. [[CrossRef](#)]
29. Chen, K.; Liu, S.Q.; Zhang, Q.Y. Degradation and detection of endocrine disruptors by laccase-mimetic polyoxometalates. *Front. Chem.* **2022**, *10*, 854045. [[CrossRef](#)]
30. Ma, Y.; Xue, Q.; Min, S.T.; Zhang, Y.P.; Hu, H.M.; Gao, S.L.; Xue, G.L. An unusual fan-type polyanion with a silver cation located at the axial center, [AgAs^{III}₂(As^{III}As^VMo₄O₁₈(OH)₂)₃]¹¹⁻. *Dalton Trans.* **2013**, *42*, 3410–3416. [[CrossRef](#)]
31. Li, F.Y.; Xu, L. Coordination assemblies of polyoxomolybdate cluster framework: From labile building blocks to stable functional materials. *Dalton Trans.* **2011**, *40*, 4024–4034. [[CrossRef](#)] [[PubMed](#)]
32. Chen, X.X.; Wang, Z.; Zhang, R.R.; Xu, L.Q.; Sun, D. A novel polyoxometalate-based hybrid containing a 2D [CoMo₈O₂₆]_∞ structure as the anode for lithium-ion batteries. *Chem. Commun.* **2017**, *53*, 10560–10563. [[CrossRef](#)] [[PubMed](#)]
33. Hua, J.A.; Wei, X.M.; Ma, X.; Jiao, J.Z.; Chai, B.H.; Wu, C.B.; Zhang, C.L.; Niu, Y.L. A {Cd₄Cl₂O₁₄} cluster functionalized sandwich-type tungstoarsenate as a conformation modulator for misfolding Aβ peptides. *CrystEngComm* **2022**, *24*, 1171–1176. [[CrossRef](#)]
34. Chaudhary, H.; Iashchishyn, I.A.; Romanova, N.V.; Rambaran, M.A.; Musteikyte, G.; Smirnovas, V.; Holmboe, M.; Ohlin, C.A.; Svedruzic, Z.M.; Morozova-Roche, L.A. Polyoxometalates as effective nano-inhibitors of amyloid aggregation of pro-inflammatory S100A9 protein involved in neurodegenerative diseases. *ACS Appl. Mater. Interfaces* **2021**, *13*, 26721–26734. [[CrossRef](#)] [[PubMed](#)]
35. Shao, X.; Yan, C.R.; Wang, C.; Wang, C.L.; Cao, Y.; Zhou, Y.; Guan, P.; Hu, X.L.; Zhu, W.L.; Ding, S.C. Advanced nanomaterials for modulating Alzheimer’s related amyloid aggregation. *Nanoscale Adv.* **2023**, *5*, 46–80. [[CrossRef](#)]
36. Hua, J.A.; Wang, F.; Wei, X.M.; Qin, Y.X.; Lian, J.M.; Wu, J.H.; Ma, P.T.; Ma, X. A nanoenzyme constructed from manganese and Strandberg-type phosphomolybdate with versatility in antioxidant and modulating conformation of Aβ protein misfolding aggregates in vitro. *Int. J. Mol. Sci.* **2023**, *24*, 4317. [[CrossRef](#)]
37. Zhang, Z.Z.; Hu, G.H.; Yan, X. Hydrothermal synthesis, structure and properties of a new phosphomolybdate based on novel [Co(H₂O)₄(HP₂Mo₅O₂₃)]⁸⁻ anions and [H₈(H₂O)₁₆]⁸⁺ water cluster cations. *Chem. Res. Chin. Univ.* **2016**, *32*, 329–333. [[CrossRef](#)]
38. Hua, J.A.; Wei, X.M.; Zhang, N.; Chen, P.J.; Ma, X. Synthesis of a linear cobalt-substituted strandberg-type polyphosphomolybdate with ability in modulating conformation of Aβ-peptide misfolding aggregation. *Chin. J. Inorg. Chem.* **2022**, *38*, 1908–1918.
39. Zheng, S.T.; Zhang, J.; Juan, J.M.; Yuan, D.Q.; Yang, G.Y. Poly(polyoxotungstate)s with 20 nickel centers: From nanoclusters to one-dimensional chains. *Angew. Chem. Int. Ed. Engl.* **2009**, *48*, 7176–7179. [[CrossRef](#)]
40. Brown, I.D.; Altermatt, D. Bond-valence parameters obtained from a systematic analysis of the inorganic crystal structure database. *Acta Crystallogr. B Struct. Sci.* **1985**, *41*, 244–247. [[CrossRef](#)]
41. Shields, G.P.; Raithby, P.R.; Allen, F.H.; Motherwell, W.D.S. The assignment and validation of metal oxidation states in the Cambridge structural database. *Acta Crystallogr. B Struct. Sci.* **2000**, *56*, 455–465. [[CrossRef](#)] [[PubMed](#)]

42. Streb, C.; Ritchie, C.; Long, D.L.; Kögerler, P.; Cronin, L. Modular assembly of a functional polyoxometalate-based open framework constructed from unsupported AgI–AgI interactions. *Angew. Chem. Int. Ed. Engl.* **2007**, *46*, 7579–7582. [[CrossRef](#)] [[PubMed](#)]
43. Ma, X.; Wei, X.M.; Wang, M.; Zhang, N.; Chen, P.J.; Hua, J.A. A hexa-Cu cluster sandwiched silicotungstate with reactive oxygen species catalytic ability and anti-tumor activity in PC12 cells. *J. Mol. Struct.* **2022**, *1267*, 133616. [[CrossRef](#)]
44. Ma, X.; Sun, Y.S.; Lu, Q.L.; Bai, X.Q.; Zang, Q.J.; Yan, X.W.; Wang, F.; Hua, J.A. A nanoscale ferromagnetic nickel-supercluster functionalized giant heterometallic arsenotungstate with ability in catalyzing reactive oxygen species generation. *J. Mol. Struct.* **2023**, *1291*, 136010. [[CrossRef](#)]
45. Feng, S.L.; Lu, Y.; Zhang, Y.X.; Su, F.; Sang, X.J.; Zhang, L.C.; You, W.S.; Zhu, Z.M. Three new Strandberg-type phenylphosphomolybdate supports for immobilizing horseradish peroxidase and their catalytic oxidation performances. *Dalton. Trans.* **2018**, *47*, 14060–14069. [[CrossRef](#)] [[PubMed](#)]
46. Gao, Y.; Chen, Y.; Wang, C.Y.; Yin, A.P.; Li, H.L.; Zhao, J.S. Polyoxometalates encapsulated into hollow periodic mesoporous organosilica as nanoreactors for extraction oxidation desulfurization. *Catalysts* **2023**, *13*, 747. [[CrossRef](#)]
47. Yang, D.H.; Li, S.Z.; Ma, P.T.; Wang, J.P.; Niu, J.Y. Carboxylate-functionalized phosphomolybdates: Ligand-directed conformations. *Inorg. Chem.* **2013**, *52*, 8987–8992. [[CrossRef](#)]
48. Ma, X.; Wang, Y.Q.; Hua, J.A.; Xu, C.Y.; Yang, T.; Yuan, J.; Chen, G.Q.; Guo, Z.J.; Wang, X.Y. A β -sheet-targeted theranostic agent for diagnosing and preventing aggregation of pathogenic peptides in Alzheimer's disease. *Sci. China Chem.* **2020**, *63*, 73–82. [[CrossRef](#)]
49. Barnham, K.J.; Bush, A.I. Biological metals and metal-targeting compounds in major neurodegenerative diseases. *Chem. Soc. Rev.* **2014**, *43*, 6727–6749. [[CrossRef](#)]
50. Gao, N.; Liu, Z.; Zhang, H.; Liu, C.; Yu, D.; Ren, J.; Qu, X. Site-directed chemical modification of amyloid by polyoxometalates for inhibition of protein misfolding and aggregation. *Angew. Chem. Int. Ed.* **2022**, *61*, e202115336. [[CrossRef](#)]
51. Wang, X.H.; Wang, X.Y.; Zhang, C.L.; Jiao, Y.; Guo, Z.J. Inhibitory action of macrocyclic platinumiferous chelators on metal-induced A β aggregation. *Chem. Sci.* **2012**, *3*, 1304–1312. [[CrossRef](#)]
52. Kozłowski, H.; Janicka-Kłos, A.; Brasun, J.; Gaggelli, E.; Valensin, D.; Valensin, G. Copper, iron, and zinc ions homeostasis and their role in neurodegenerative disorders (metal uptake, transport, distribution and regulation). *Coordin. Chem. Rev.* **2009**, *253*, 2665–2685. [[CrossRef](#)]
53. Noël, S.; Cadet, S.; Gras, E.; Hureau, C. The benzazole scaffold: A SWAT to combat Alzheimer's disease. *Chem. Soc. Rev.* **2013**, *42*, 7747–7762. [[CrossRef](#)]
54. Palanimuthu, D.; Wu, Z.; Jansson, P.J.; Braidy, N.; Bernhardt, P.V.; Richardson, D.R.; Kalinowski, D.S. Novel chelators based on adamantane-derived semicarbazones and hydrazones that target multiple hallmarks of Alzheimer's disease. *Dalton Trans.* **2018**, *47*, 7190–7205. [[CrossRef](#)] [[PubMed](#)]
55. SAINT; Bruker AXS Inc.: Madison, WI, USA, 2007.
56. Brese, N.E.; O'Keeffe, M. Bond-valence parameters for solids. *Acta Crystallogr. B Struct. Sci.* **1991**, *47*, 192–197. [[CrossRef](#)]
57. Sheldrick, G.M. *SHELXTL-97*; Programs for crystal structure refinements; University of Göttingen: Göttingen, Germany, 1997.
58. Li, M.; Howson, S.E.; Dong, K.; Gao, N.; Ren, J.S.; Scott, P.; Qu, X.G. Chiral metallohelical complexes enantioselectively target amyloid- β for treating Alzheimer's disease. *J. Am. Chem. Soc.* **2014**, *136*, 11655–11663. [[CrossRef](#)] [[PubMed](#)]

Disclaimer/Publisher's Note: The statements, opinions and data contained in all publications are solely those of the individual author(s) and contributor(s) and not of MDPI and/or the editor(s). MDPI and/or the editor(s) disclaim responsibility for any injury to people or property resulting from any ideas, methods, instructions or products referred to in the content.